Supporting Information

Potential alignment in tandem catalysts enhances CO_2-to-C_2H_4 conversion efficiencies

Min Liu[†,*], Qiyou Wang[†,*], Tao Luo[†], Matias Herran[η], Xueying Cao[‡], Wanru Liao[†], Li Zhu[η], Hongmei Li[†], Andrei Stefancu[η], Ying-Rui Lu[θ], Ting-Shan Chan[θ], Evangelina Pensa[η], Chao Ma[§], Shiguo Zhang[§], Ruiyang Xiao[ξ,*], Emiliano Cortés[η,*]

[†]Hunan Joint International Research Center for Carbon Dioxide Resource Utilization, State Key Laboratory of Powder Metallurgy, School of Physics and Electronics, Central South University, Changsha 410083, Hunan, China.

[η]Nanoinstitute Munich, Faculty of Physics, Ludwig-Maximilians-Universität München, 80539 München, Germany

[‡]College of Materials Science and Engineering, Linyi University, Linyi 276000, Shandong, China.

[θ]National Synchrotron Radiation Research Center, 30092, Hsinchu, Taiwan

[§]College of Materials Science and Engineering, Hunan University, Changsha 410082, P. R. China

[ξ]Institute of Environmental Engineering, School of Metallurgy and Environment, Central South University, Changsha 410083, China

*Corresponding authors: minliu@csu.edu.cn, qiyouwang@csu.edu.cn, xiao.53@csu.edu.cn, Emiliano.Cortes@lmu.de

Table of Contents

Materials and Methods

Computational details. All our investigations in this study are based on spin-polarized density functional theory, as implemented in the Vienna ab initio simulation package (VASP)[1]. The exchange-correlation potential is treated with the Perdew-Burke-Ernzerhof (PBE) formula by using the projected augmented wave (PAW) method within the generalized gradient approximation (GGA)[2,3]. The cut-off energy for all calculations was set to be 450 eV. All the positions of atoms are fully relaxed until the Hellmann-Feynman forces on each atom are less than 0.01 eV/Å. Meanwhile, a k-points Γ-centered mesh is generated for Brillouin zone samples. The DFT-D3 method proposed by Grimme was adopted to describe the van der Waals interactions, which has been shown to accurately describe chemisorption and physisorption properties on layered material. In addition, a vacuum region of about 15 Å was used to decouple the periodic replicas. Cu (111) were modelled with a periodic four-layer p (6 × 6) model with the two lower layers fixed and the two upper layers relaxed. The lattice parameters of this slab are a = 10.10 Å, b = 10.10 Å and b = 21.20 Å after optimization. We also used the VESTA package to visualize the structures and charge density differences[4].

The relative activation barriers for C-C coupling on the Cu (111) surface can be calculated by

$$\Delta E_{reaction} = \Delta E_{coco} - \Delta E_{co+co}$$

where ΔE_{coco} and ΔE_{co+co} are the total system total energy calculated by DFT after C-C coupling and before C-C coupling, respectively

Chemicals. Dicyandiamide (DCDA), NaCl, KCl, 4-Aminophthalonitrile, nickel acetate tetrahydrate, $NiCl_2$, Ag nanoparticles (NPs), sodium borohydride ($NaBH_4$) and $CuSO_4 \cdot 5H_2O$ were bought from Shanghai Aladdin reagent Co. Ltd. Carbon nanotube-1 (CNT-1, 30-50 nm in diameter) and Carbon nanotube-2 (CNT-2, 10-20 nm in diameter) were purchased from Pioneer Nanotechnology Co. Ltd and Tanfeng technology. Inc., respectively. Before using the CNTs, 0.5 M HNO_3 was used to remove the potential metal impurities in 80 ^{o}C for 12 hours.

Synthesis of Ni SAC. The C_3N_4 nanosheets was prepared based on our previous studies[5]. Then 0.02 g C_3N_4 nanosheets and 0.04 g CNT-1 were added to 30 mL DI water. C_3N_4 nanosheets were spread out and shattered uniformly through 60 min ultrasound. 0.05 mL of 0.1 M $NiCl_2$ was added dropwise to the mixture followed by stirring for 2h. The liquid nitrogen was poured directly into the mixed solution until icing totally. After freeze-dried for 72h, the aerogel was obtained. Then the aerogel was heated to 750 ^oC with a 5 ^oC/min heating rate at Ar atmosphere, immediately followed by colling at 10 ^oC/min to room temperature.

Synthesis of Ni Pc catalyst. 4 mmol of 4-Aminophthalonitrile and 1 mmol of nickel acetate tetrahydrate were dissolved into 30 mL of ethanol under ultrasonic treatment. The mixture was transferred into a 50 mL Teflon-lined stainless-steel autoclave and then heated at 160 ^oC for 6 h to obtain Ni Pc catalyst precursor. 0.03 mmol Ni Pc catalyst precursor and 100 mg of CNT-2 was dispersed into 50 mL of DMF followed by 30 min ultrasound. The mixed suspension was further sonicated for another 30 min and stirred for 24 h at room temperature. Finally, the final Ni Pc catalyst was obtained by filtration and dried in a vacuum oven at 80 ^oC for 10 h.

Synthesis of Cu-R catalyst. Cu-R catalyst was synthesized via one-step wet chemical reduction using $CuSO_4 \cdot 5H_2O$ and $NaBH_4$ as precursors. 0.002 mol $CuSO_4 \cdot 5H_2O$ and 0.04 mol $NaBH_4$ were added into 10 mL and 40 mL DI water, respectively. Next, $CuSO_4$ solution was injected rapidly into the $NaBH_4$ solution under 600r stirring. Then the precipitate obtained was subsequently washed three times and once with ethanol to completely remove the unreacted precursors, followed by being immediately dried under vacuum overnight.

Synthesis of Ni SAC+Cu-R catalyst. The Ni SAC+Cu-R catalyst was prepared through facile nanoscale-mixing. Briefly, 0.1 mg Ni SAC and 2 mg Cu-R were firstly mixed with 10 mL of isopropanol under intense stirring at room temperature. After 30 min ultrasonic treatment, the mixture was put into the rotary evaporator to remove isopropanol.

Synthesis of Ni Pc+Cu-R catalyst. 0.1 mg Ni Pc and 2 mg Cu-R were firstly mixed

with 10 mL of isopropanol under intense stirring at room temperature. After 30 min ultrasonic treatment, the mixture was put into the rotary evaporator to remove isopropanol.

Synthesis of Ag+Cu-R catalyst. 0.1 mg Ag Nanoparticles and 2 mg Cu-R were firstly mixed with 10 mL of isopropanol under intense stirring at room temperature. After 30 min ultrasonic treatment, the mixture was put into the rotary evaporator to remove isopropanol.

Characterizations. Powder X-ray diffraction (XRD) patterns were collected by using a D8 advance X-ray diffractometer (Rigaku, Japan) with Cu Kα radiation (λ = 0.15406 nm) at a scan rate (2θ) of 5 °/min. The morphologies of the samples were determined by TESCAN MIRA3 field emission scanning electron microscope (LMH) and high-resolution transmission electron microscopy with a spherical aberration corrector (HRTEM, Titan G2 60-300) equipped with energy dispersive X-ray spectroscopy (EDS) mapping. The atomically dispersed metal atoms were detected by Aberration-corrected HAADF-STEM (JEM-ARM200F). Ni X-ray absorption spectra were obtained at beamlines 01C1 of the National Synchrotron Radiation Research Center (NSRRC, Taiwan). X-ray photoelectron spectroscopy (XPS) measurements were performed on Thermo Fisher Scientific Escalab 250 XI, and all the binding energies were calibrated by the C 1*s* peak at 284.5 eV. Inductively Coupled Plasma Mass Spectrometry (ICP-MS, Agilent 7700s) was used to measure the content of Ni atoms in the SAC. The gas phase products after bulk electrolysis were quantified by on-line Gas chromatograph (GC, Shimidzu, Model 2014).

Electrochemical measurements. All electrochemical measurements in this study were operated on a typical three electrode system using the electrochemical workstation (AUT50783). The flow-cell reactor measurements were performed on a home-made cell including sandwich of flow frames, gaskets, and an anion-exchange membrane (Selemion DSVN). In the flow-cell reactor, 6 mg catalyst was mixed with 950 μL isopropanol, 150 μL PTFE solution (Polytetrafluoroethylene, 1 wt%) and 24 μL nafion solutions (5 wt%, Sigma-Aldrich) followed by sonication of 30 min to form a

homogenous solution. The obtained catalyst ink was dropped onto hydrophobic porous polytetrafluoroethylene gas diffusion electrode (GDE) (1 cm× 3 cm) directly and then dried at 70 °C for 8 hours. The loading of catalyst is 2 mg/cm^2 and the area contacting with electrolyte is 0.5 cm^2. the IrO_2–coating titanium sheet is used as counter electrode and an Ag/AgCl (with saturated 3.5 M KCl) electrode as a reference electrode. The flow rate of the electrolyte (1 M $KHCO_3$) was set at 30 mL/min in both of cathodic and anodic chambers. Galvanostatic test was conducted for analyze the faradic efficiency. All potentials were referenced to reversible hydrogen electrode (RHE) with the formula of E (RHE) = E (Ag/AgCl, 3.5M KCl) + 0.205 V + 0.059 V × pH after *iR* compensation. The products from cathodic were analyzed by an on-line gas chromatograph. High-purity N_2 (99.999%) was used as the carrier gas. A TCD was used to measure the H_2 fraction and a flame ionization detector was equipped with a nickel conversion furnace to analyze the CO and C_2H_4 fraction. The faradaic efficiency of products was calculated from gas chromatograph chromatogram peak according to the flowing equation:

$$FE = \frac{V \times n \times S \times F \times P}{iRT} \times 100\%$$

V: the volume of the target product of the 1 mL sample detected by the GC

n: the number of transferred electrons of the target product

S: the gas flow rate, 20 mL/min

F: faraday constant (96485 C/mol)

P: normal atmosphere (101325 Pa)

I: applied current

R: gas constant (8.314 J/(mol·K))

T: room temperature (298 K)

***In situ* attenuated total reflection-infrared spectroscopy (ATR-IR).** ATR-IR was carried out on a Nicolet iS50 FT-IR spectrometer equipped with an MCT detector cooled with liquid nitrogen. First, the Si prism was polished with a slurry of 0.3 μm Al_2O_3 and sonicated in acetone and deionized water. After polishing, the Si prism was soaked in a piranha solution (3:1 volumetric ratio of 98% H_2SO_4 and H_2O_2) for 60 min

in order to clean the prism of organic contaminants. Then the reflecting surface was immersed in a mixture of the Au plating solution[6] at 60 °C for 10 min. 2 mg catalyst was mixed with 970 μL isopropanol and 30 μL Nafion solutions (5 wt%, Sigma-Aldrich) followed by sonication of 30 min to form a homogeneous solution. Then 100 μL of catalyst ink was cast onto the Au film modified Si prism reflecting surface. In situ ATR-IR spectra were recorded during stepping the working electrode potential.

Supplementary Figures

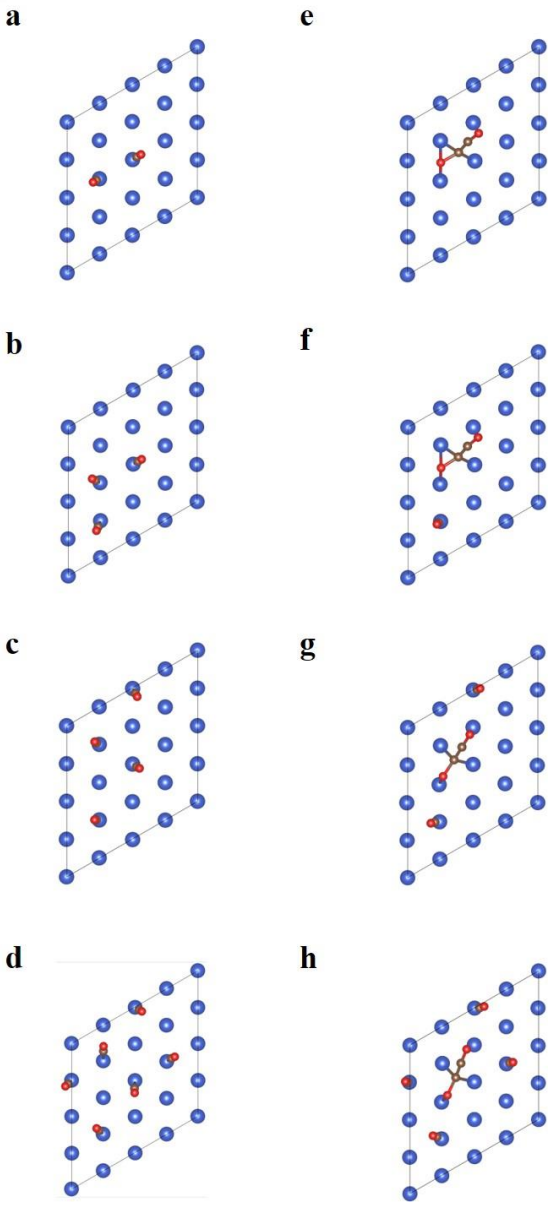

Figure S1. DFT-predicted *CO on a Cu (111) surface with (a) no additional *CO, (b) one *CO, (c) two *CO and (c) four *CO. *OCCO geometries on a Cu (111) surface with (e) no additional *CO, (f) one *CO, (g) two *CO and (h) four *CO.

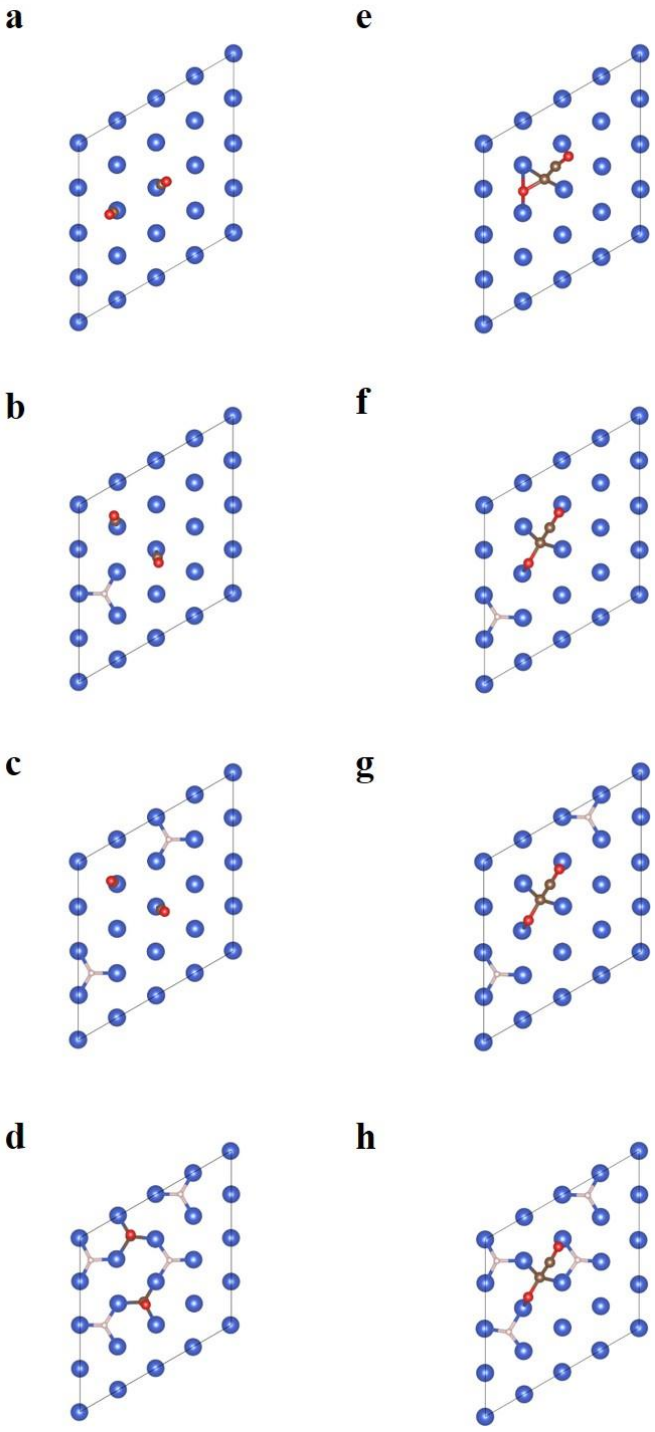

Figure S2. DFT-predicted *CO on a Cu (111) surface with (a) no additional *H, (b) one *H, (c) two *H and (c) four *H. *OCCO geometries on a Cu (111) surface with (e) no additional *H, (f) one *H, (g) two *H and (h) four *H.

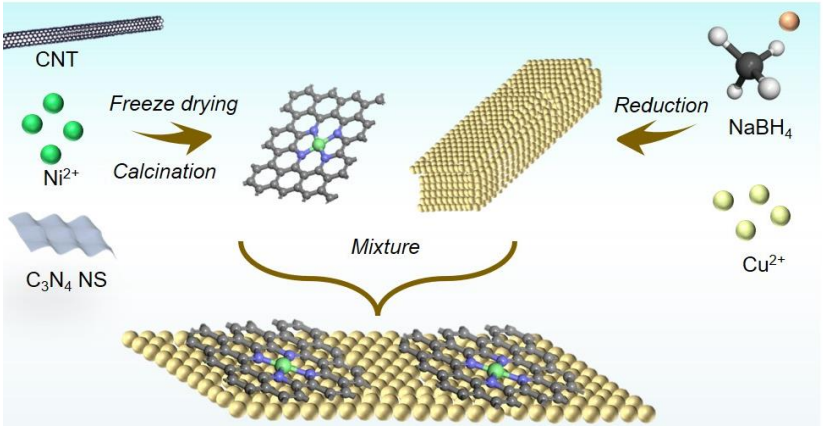

Figure S3. Schematic illustration of the preparation for Ni SAC+Cu-R.

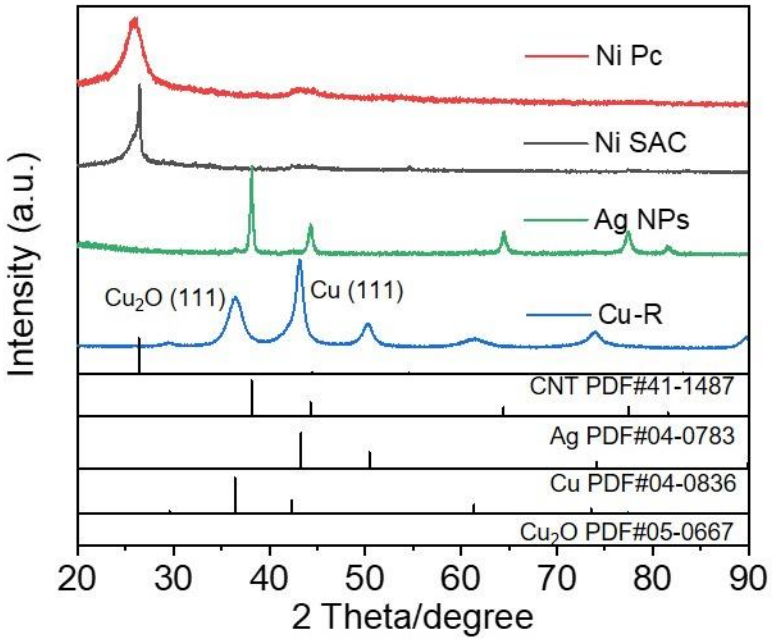

Figure S4. XRD patterns of catalysts.

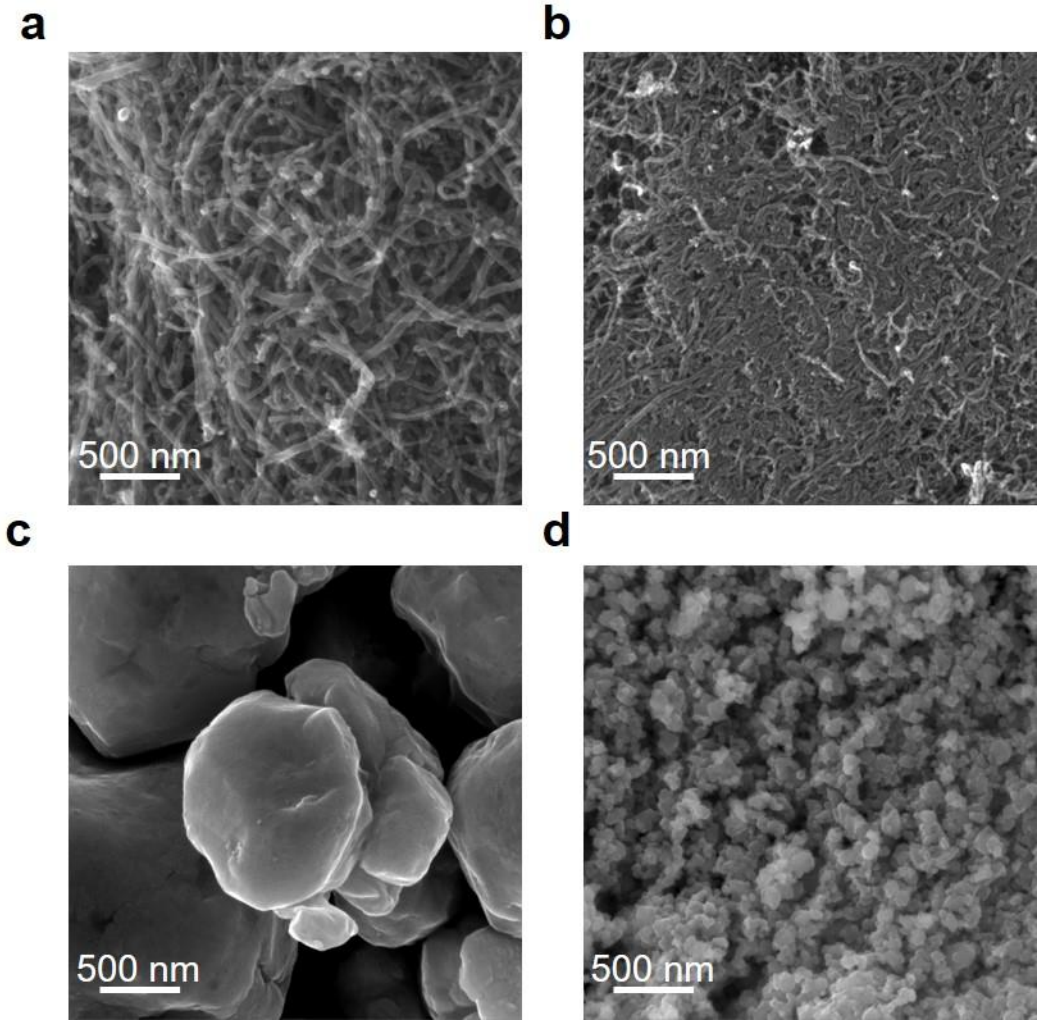

Figure S5. SEM images of catalysts. (a) Ni SAC. (b) Ni Pc. (c) Ag NPs. (d) Cu-R.

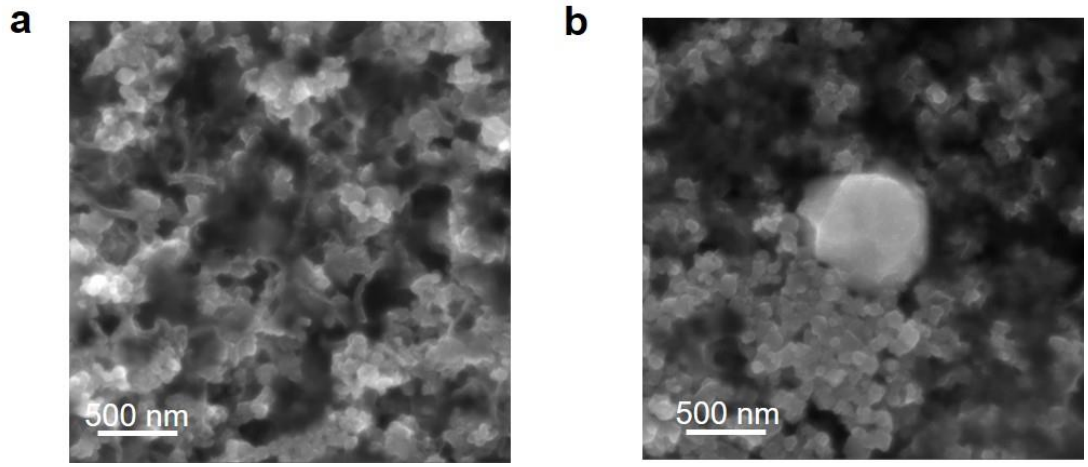

Figure S6. SEM images of catalysts. (a) Ni Pc+Cu-R. (b) Ag NPs+Cu-R.

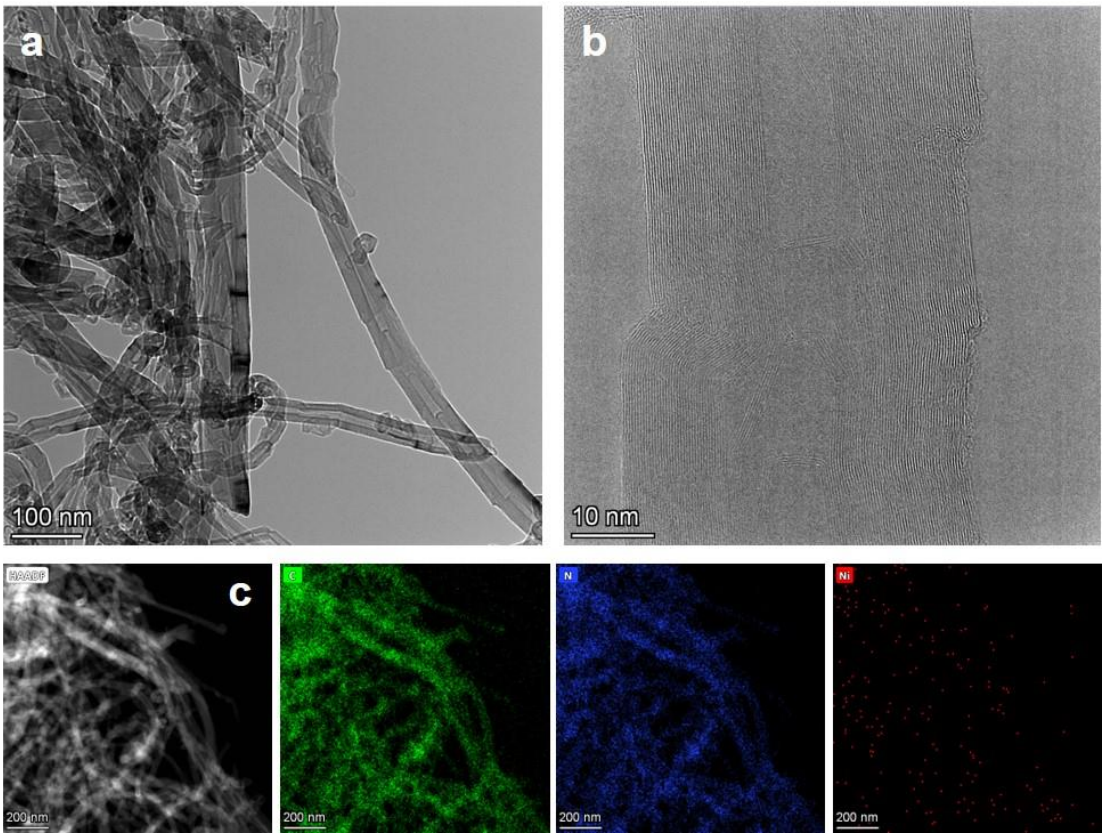

Figure S7. (a) TEM image of Ni SAC. (b) HRTEM image of Ni SAC. (c) EDS mapping image Ni SAC.

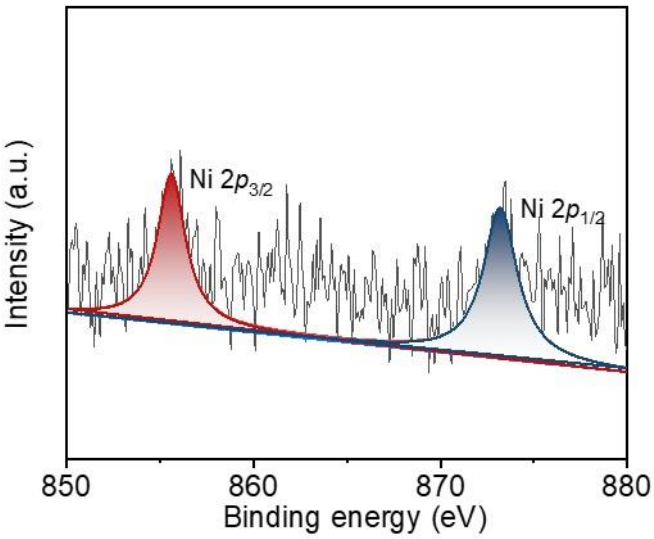

Figure S8. High-resolution XPS spectra of Ni 2*p* for Ni SAC.

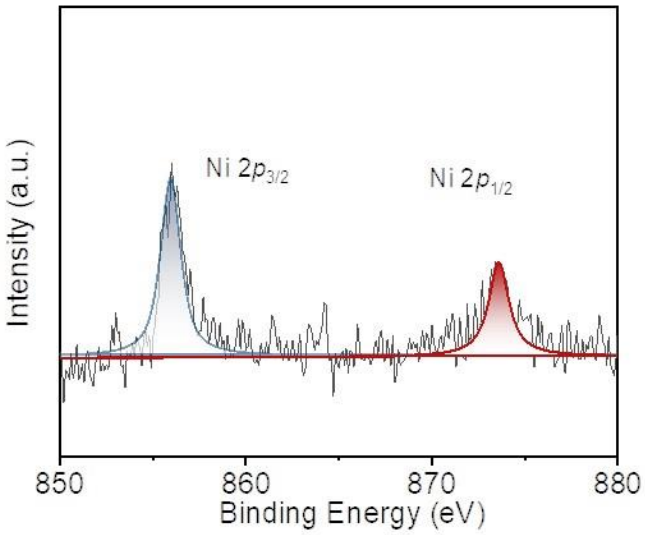

Figure S9. High-resolution XPS spectra of Ni 2*p* for Ni Pc.

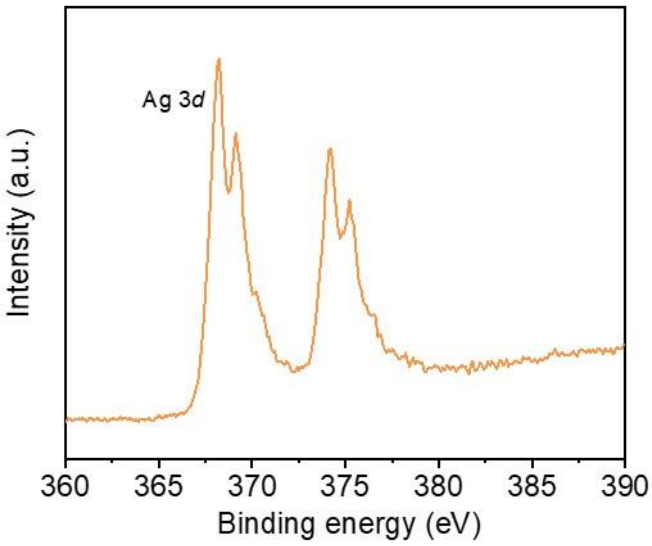

Figure S10. High-resolution XPS spectra of Ag 3*d* for Ag NPs.

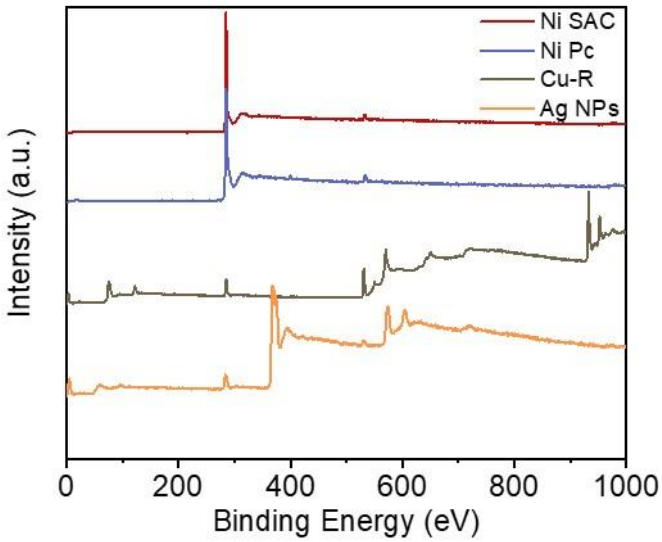

Figure S11. Survey and high-resolution XPS spectra of catalysts.

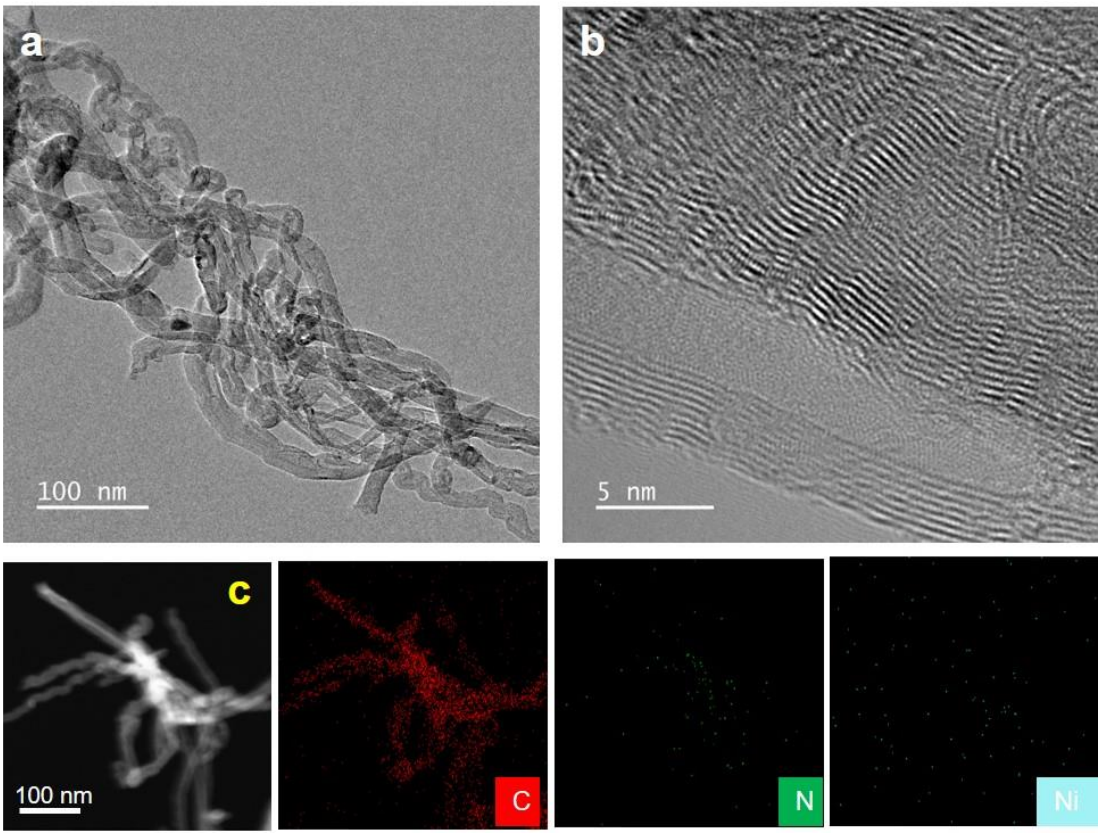

Figure S12. (a) TEM image of Ni Pc. (b) HRTEM image of Ni Pc. (c) EDS mapping image of Ni Pc.

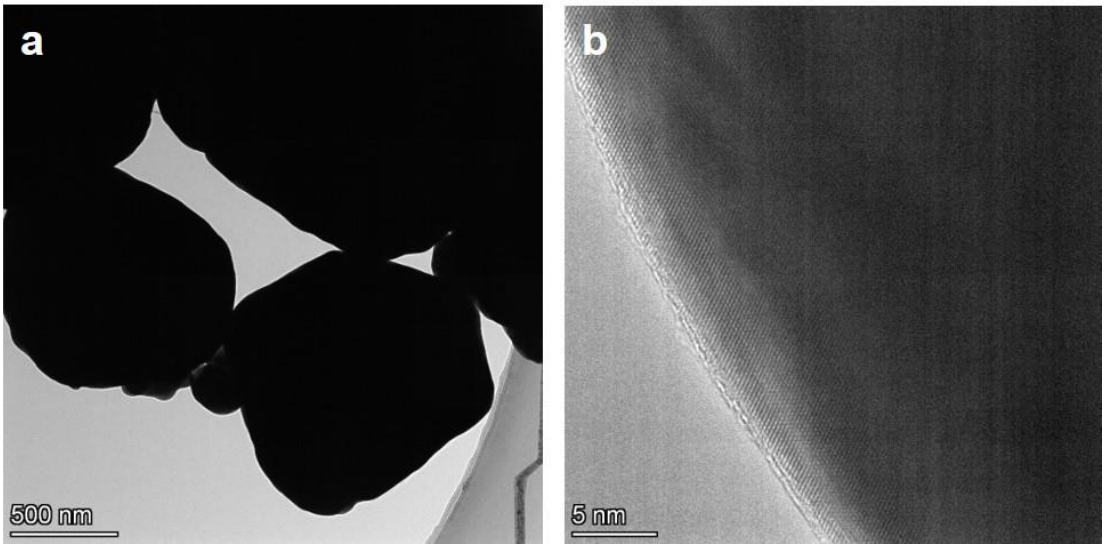

Figure S13. (a) TEM image of Ag NPs. (b) HRTEM image of Ag NPs.

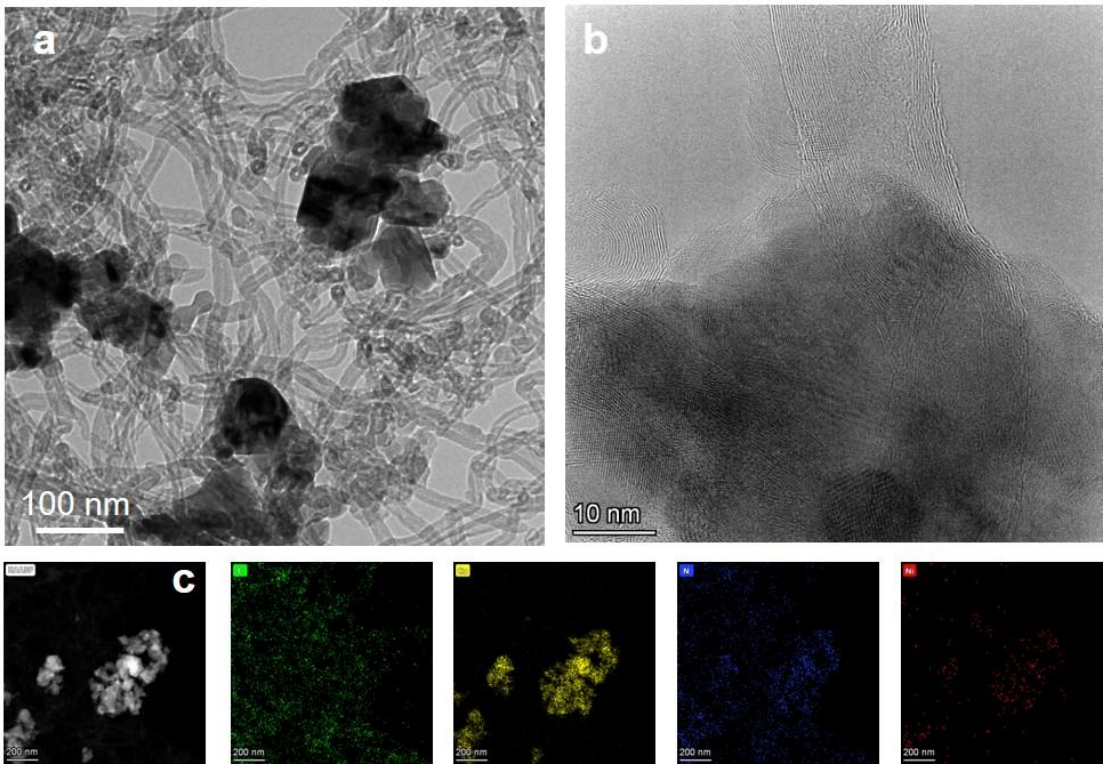

Figure S14. (a) TEM image of Ni Pc+Cu-R. (b) HRTEM image of Ni Pc+Cu-R. (c) EDS mapping image of Ni Pc+Cu-R.

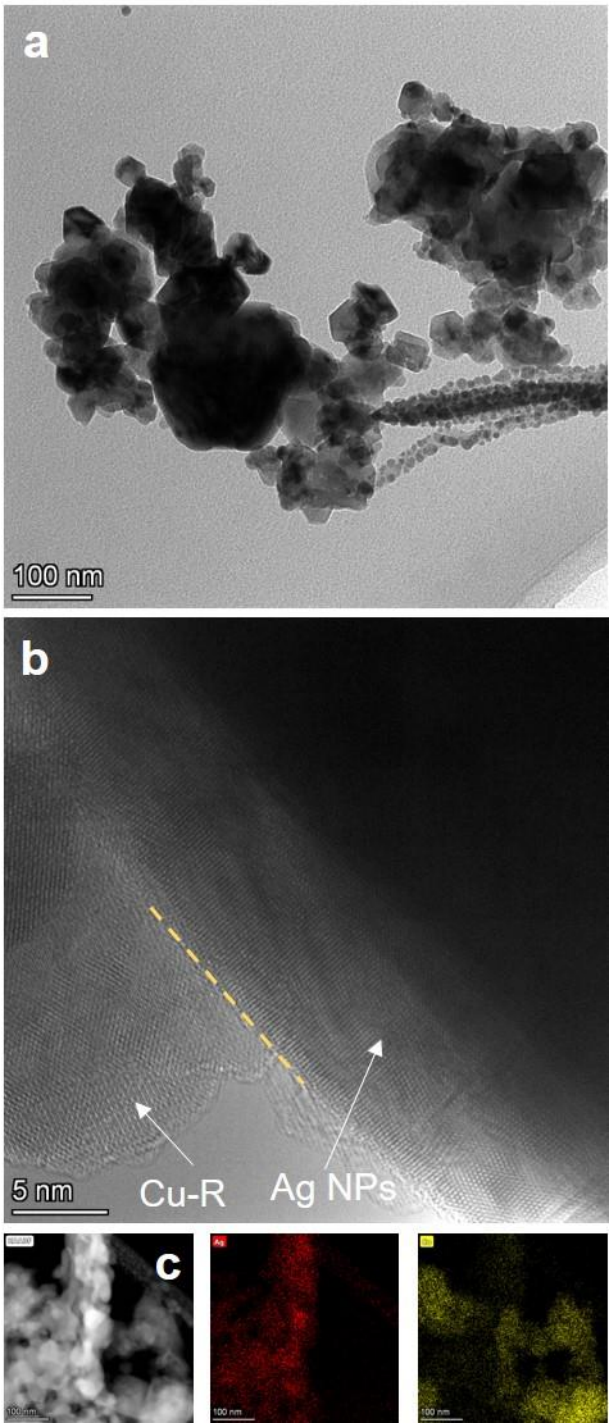

Figure S15. (a) TEM image of Ag+Cu-R. (b) HRTEM image of Ag+Cu-R. (c) EDS mapping image of Ag+Cu-R.

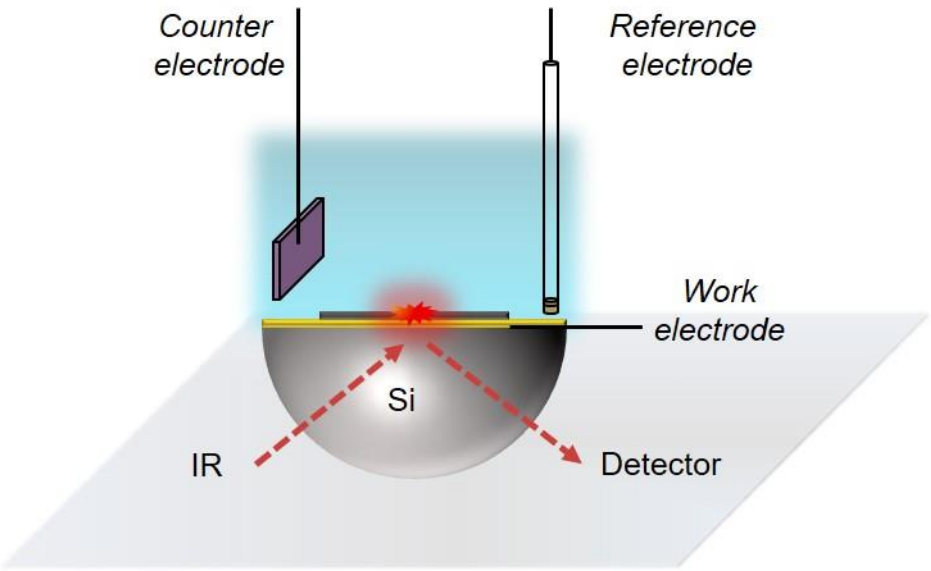

Figure S16. Schematic representation of attenuated total reflection surface-enhanced infrared absorption spectroscopy (ATR-SEIRAS).

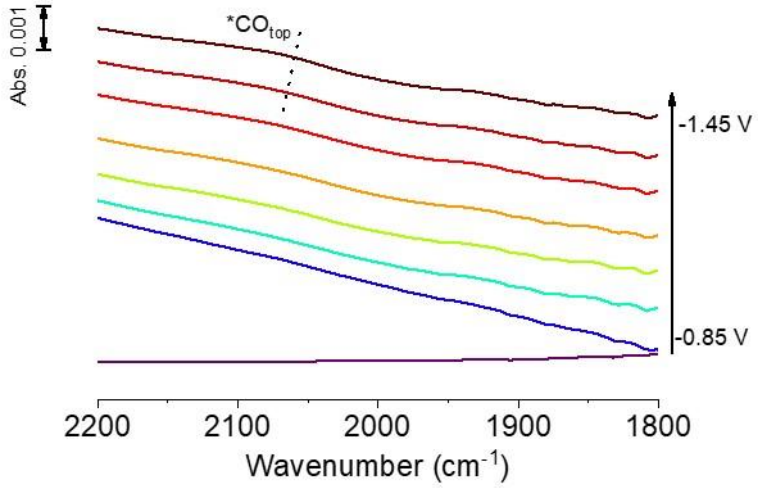

Figure S17. *In situ* ATR-IR spectra of Ag+Cu-R.

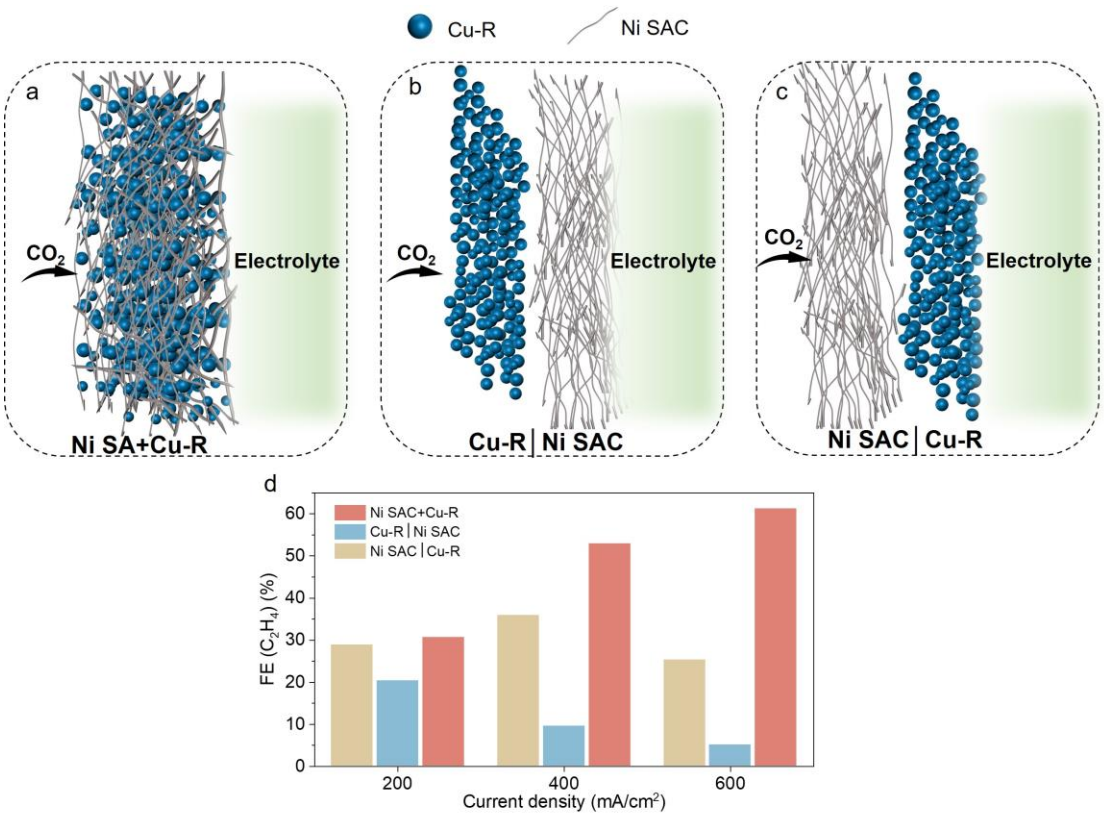

Figure S18. Schematic diagram for the structure of a) Ni SAC+Cu-R, b) Cu-R | Ni SAC and c) Ni SAC | Cu-R tandem catalysts. (d) FE_{C2H4} of each tandem catalyst.

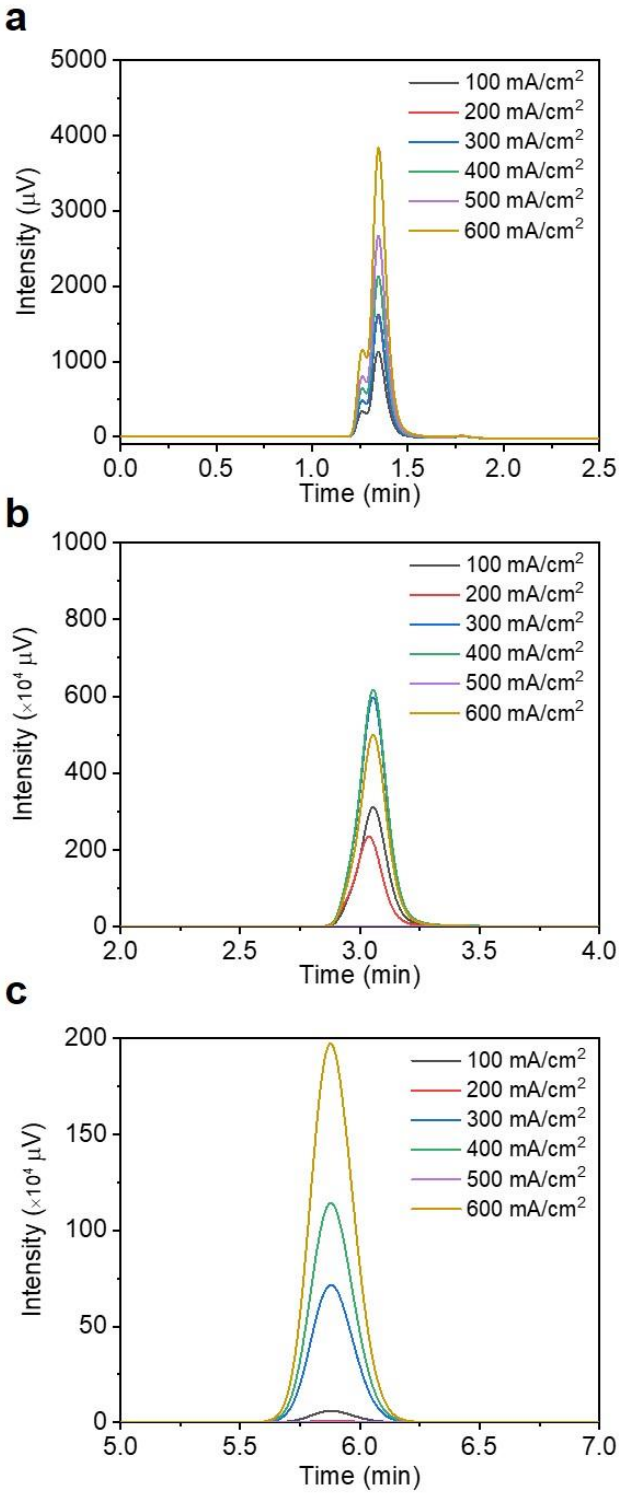

Figure S19. The spectra of Gas chromatograph (GC) for (a) H_2, (b) CO and (c) C_2H_4 produced by Ni SAC+Cu-R catalyst.

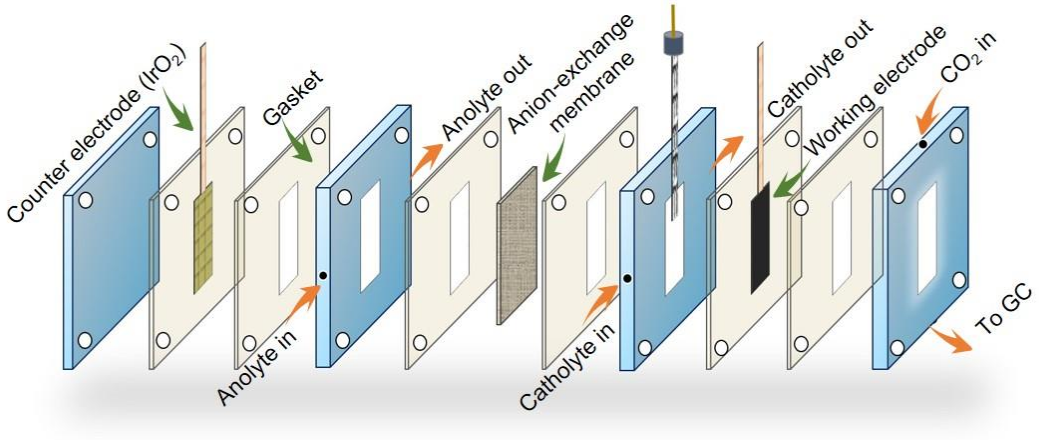

Figure S20. Schematic representation of electrode on flow-cell reactor.

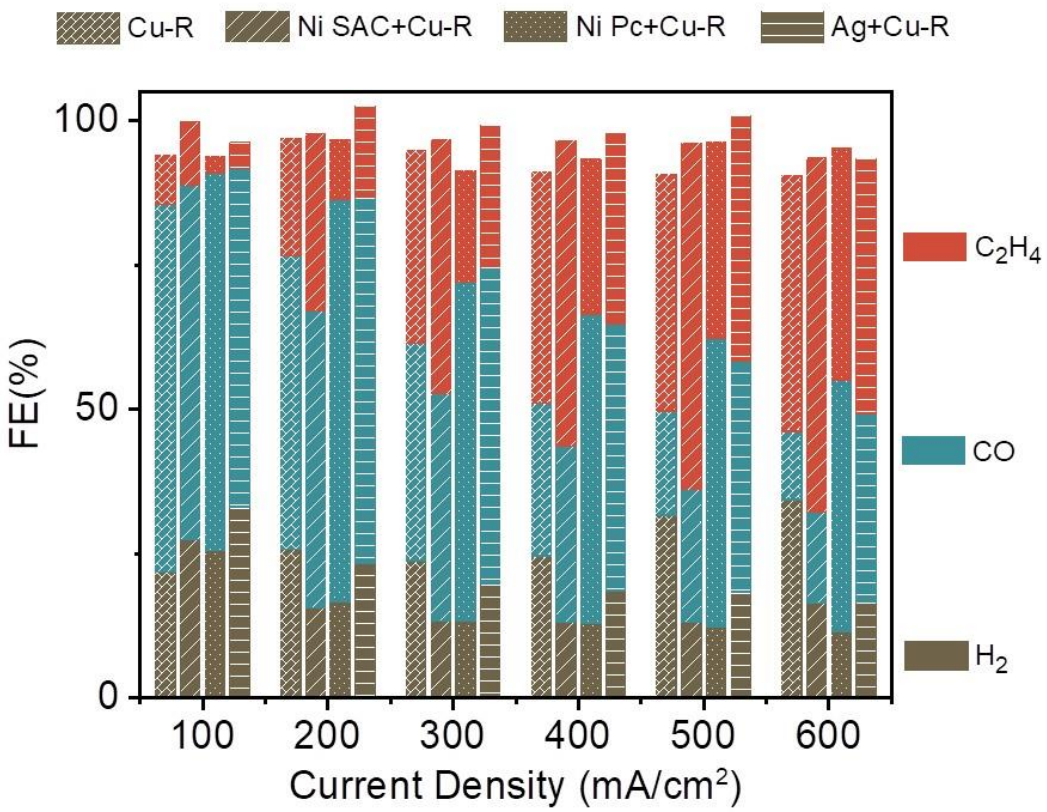

Figure S21. Product distribution and corresponding FEs of catalysts.

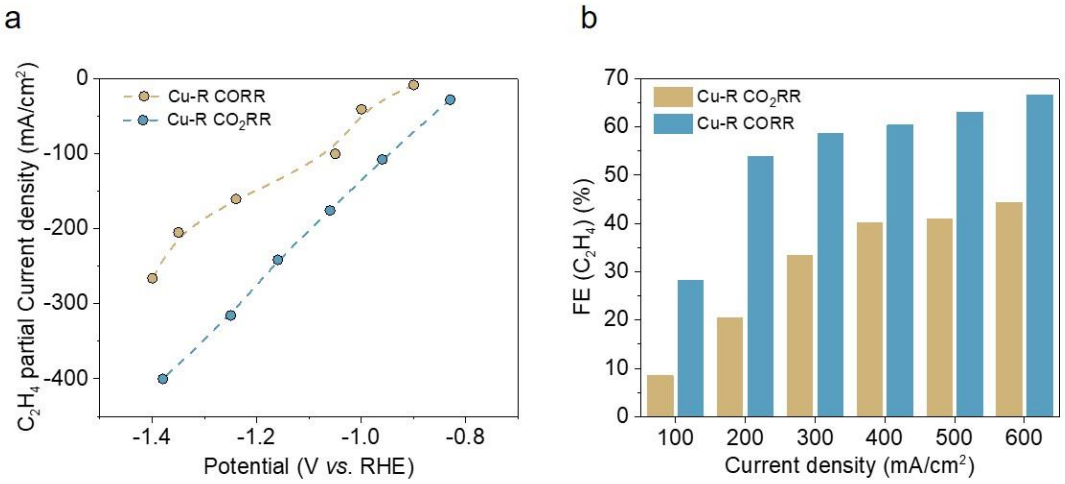

Figure S22. (a) The partial current densities of C_2H_4 at different potentials of catalysts in flow-cell reactor during CO_2RR and CORR. (b) FE_{C2H4} of tandem catalysts during CO_2RR and CORR.

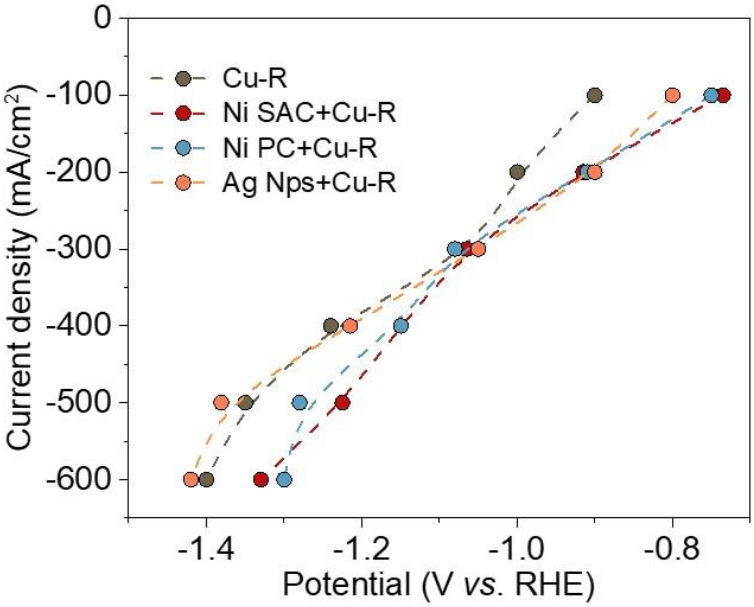

Figure S23. The total current densities of catalyst at different potentials in flow-cell reactor.

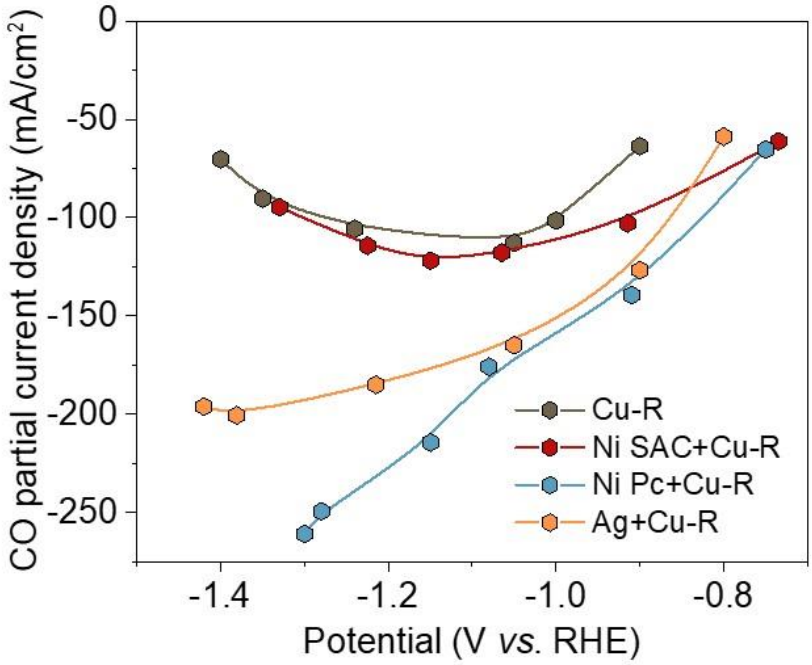

Figure S24. The partial current densities of CO at different potentials of catalysts in flow-cell reactor.

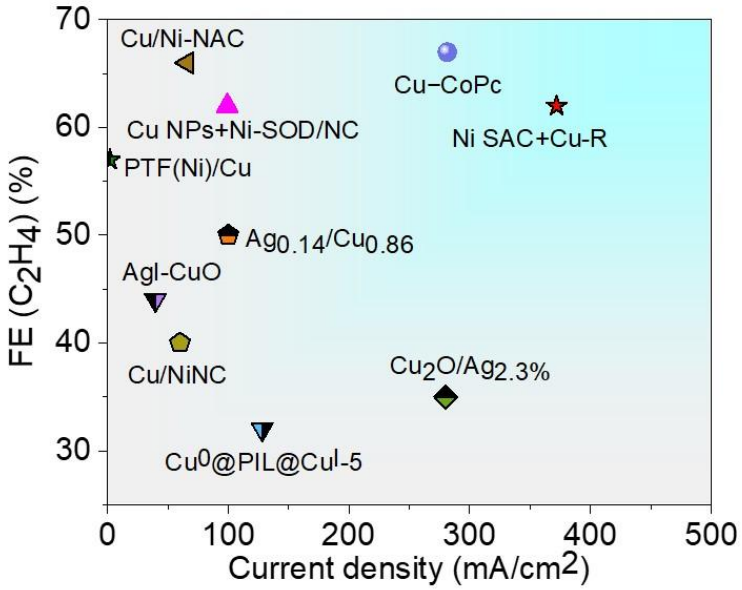

Figure S25. Performance comparison of tandem efficiencies for different tandem catalysts for CO_2RR to C_2H_4 [7-15]. The system investigated in this study is shown with a red star, highlighting the 62% selectivity obtained even at high current densities.

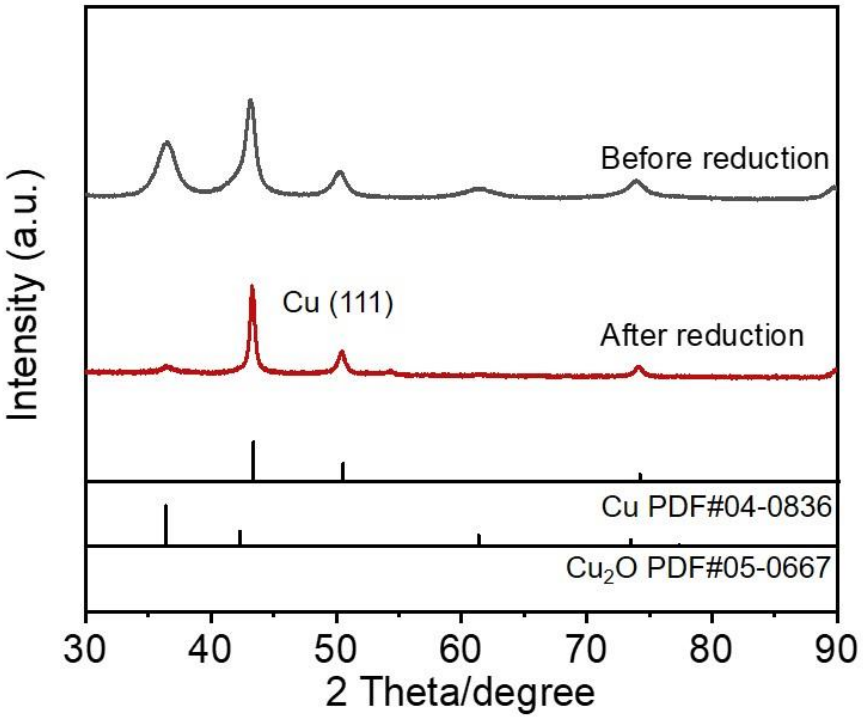

Figure S26. XRD patterns of Ni SAC+Cu-R catalyst before and after CO_2RR.

Table S1. Performance comparison of different tandem catalysts for CO_2RR to C_2H_4.

Tandem Catalysts	The current density of C_2H_4 (j_{C2H4}) (mA/cm^2)	The enhanced current density of C_2H_4 (j_{C2H4}) (mA/cm^2)	The maximal FE_{C2H4}	Ref.
Ni SAC+Cu-R	~372	~172	~62%	This work
Cu NPs+Ni-SOD/NC	~100	~56	~62%	*Angew. Chem. Int. Ed.* **2023**, *62, e202215406*
Cu^0@PIL@Cu^I-5	~128	~72	~32%	*Angew. Chem. Int. Ed.* **2022**, *61*, e202110657
AgI-CuO	~40	~31	~49%	*Angew. Chem. Int. Ed.* **2022**, *61*, e202116706
Cu/Ni-NAC	~66	~42	~66%	*J. Am. Chem. Soc.* **2022**, *144,* 20931
Cu/NiNC	~60	~24	~40%	*Adv. Funct. Mater.* **2022**, *32,* 2113252
Ag-Cu 5 %	~102	~87	~27%	*Appl. Catal. B Environ.* **2023**, *325*, 122310

References

[1] Kresse, G.; Hafner, Ab initio Molecular Dynamics for Liquid Metals. J. *Phys. Rev. B* **1993**, *47*, 558-561.

[2] Kresse, G.; Furthmüller, J. Efficient Iterative Schemes for ab initio Total-Energy Calculations Using a Plane-Wave Basis Set. *Phys. Rev. B* **1996**, *54*, 11169-11186.

[3] Perdew, J. P.; Burke, K.; Ernzerhof, M. Generalized Gradient Approximation Made Simple. *Phys. Rev. Lett.* **1996**, *77*, 3865-3868.

[4] Momma, K. & Izumi, F. VESTA: A Three-dimensional Visualization System for Electronic and Structural Analysis. *J. Appl. Crystallogr.* **2008**, *41*, 653–658.

[5] Wang, Q.; Dai, M.; Li, H.; Lu, Y. R.; Chan, T. S.; Ma, C.; Liu, K.; Fu, J.; Liao, W.; Chen, S.; Pensa, E.; Wang, Y.; Zhang, S.; Sun, Y.; Cortés, E.; Liu, M. Asymmetric Coordination Induces Electron Localization at Ca Sites for Robust CO_2 Electroreduction to CO. *Adv. Mater.* **2023**, *35,* 2300695.

[6] Yang, B.; Liu, K.; Li, H.; Liu, C.; Fu, J.; Li, H.; Huang, J. E.; Ou, P.; Alkayyali, T.; Cai, C.; Duan, Y.; Liu, An, H.; P.; Zhang, N.; Li, W.; Qiu ,X.; C. J, Jia,. L, Hu,. Z, Chai,. Lin, Y. Gao, M. Miyauchi, E. Cortés, S. A. Maier, M. Liu, Accelerating CO_2 electroreduction to multicarbon products via synergistic electric-thermal field on copper nanoneedles. *J. Am. Chem. Soc.* **2022**, *144*, 3039-3049.

[7] Yin, Z.; Yu, J.; Xie, Z.; Yu, S. W.; Zhang, L.; Akauola, T.; Chen, J. G.; Huang, Qi, W.; L.; Zhang, S. Hybrid Catalyst Coupling Single-Atom Ni and Nanoscale Cu for Efficient CO_2 Electroreduction to ethylene. *J. Am. Chem. Soc.* **2022**, *144*, 20931-20938.

[8] Lin,Y. R.; Lee, D. U.; Tan, S.; Koshy, D. M.; Lin, T. Y.; Wang, L.; Corral, D.; Avilés Acosta, J. E.; Zamora Zeledon, J. A.; Beck, V. A.; Baker, S. E.; Duoss, E. B.; Hahn, C.; Jaramillo, T. F. Vapor-Fed Electrolyzers for Carbon Dioxide Reduction Using Tandem Electrocatalysts: Cuprous Oxide Coupled with Nickel-Coordinated Nitrogen-Doped Carbon. *Adv. Funct. Mater.* **2022**, *32*, 2113252.

[9] Chen, J.; Wang, Yang, D.; X.; Cui, W.; Sang, Zhao, X.; Z.; Wang, L.; Li, Z.; Yang, B.; Lei, L.; Zheng, J.; Dai, L.; Hou, Y. Accelerated Transfer and Spillover of Carbon Monoxide through Tandem Catalysis for Kinetics-boosted Ethylene Electrosynthesis. *Angew. Chem. Inter. Ed.* **2023**, *62*, e202215406.

[10] Meng, D. L.; Zhang, M. D.; Si, D. H.; Mao, M. J.; Hou, Y.; Huang, Y. B.; Cao, R. Highly Selective Tandem Electroreduction of CO2 to Ethylene over Atomically Isolated Nickel–Nitrogen Site/Copper Nanoparticle Catalysts. *Angew. Chem. Inter. Ed.* **2021**, *60*, 25485-25492.

[11] Kong, X.; Zhao, Ke, J.; J.; Wang, C.; Li, S.; Si, R.; Liu, B.; Zeng, J.; Geng, Z. Understanding the Effect of *CO Coverage on C-C Coupling toward CO_2 Electroreduction. *Nano Lett.* **2022**, *22*, 3801-3808.

[12] Hung, S. F.; Xu, A.; Wang, X.; Li, F.; Hsu, S. H.; Li, Y.; Wicks, J.; Cervantes, E. G.; Rasouli, A. S.; Li, Y. C.; Luo, M.; Nam, D. H.; Wang, N.; Peng, T.; Yan, Y.; Lee, G.; Sargent, E. H. A Metal-Supported Single-Atom Catalytic Site Enables Carbon Dioxide Hydrogenation. *Nat. Commun.* **2022**, *13*, 819.

[13] Wang, P.; Yang, H.; Tang, C.; Wu, Y.; Zheng, Y.; Cheng, T.; Davey, K.; Huang, X.; Qiao, S. Z. Boosting Electrocatalytic CO_2-to-Ethanol Production via Asymmetric C-C Coupling. *Nat. Commun.* **2022**, *13*, 3754.

[14] Yang, R.; Duan, J.; Dong, P.; Wen, Q.; Wu, M.; Liu, Y.; Liu, Y.; Li, H.; Zhai, T. In Situ Halogen‐Ion Leaching Regulates Multiple Sites on Tandem Catalysts for Efficient CO_2 Electroreduction to C_{2+} Products. *Angew. Chem. Inter. Ed.* **2022**, *61*, e202116706.

[15] Li, Y. C.; Wang, Z.; Yuan, T.; Nam, D. H.; Luo, M.; Wicks, J.; Chen, B.; Li, J.; Li, F.; de Arquer, F.

P. G.; Wang, Y.; Dinh, C. T.; Voznyy, O.; Sinton, D.; Sargent, E. H. Binding Site Diversity Promotes CO_2 Electroreduction to Ethanol. *J. Am. Chem. Soc.* **2019**, *141*, 8584-8591.

[16] Duan, G. Y.; Li, X. Q.; Ding, G. R.; Han, L. J.; Xu, B. H.; Zhang, S. J. Highly Efficient Electrocatalytic CO_2 Reduction to C_{2+} Products on a Poly(ionic liquid)-Based Cu^0-Cu^I Tandem Catalyst. *Angew. Chem. Inter. Ed.* **2022**, *61*, e202110657.